ACS Catalysis

Research Article

pubs.acs.org/acscatalysis

Cobalt Sulfide Nanoparticles Grown on Nitrogen and Sulfur Codoped Graphene Oxide: An Efficient Electrocatalyst for Oxygen Reduction and Evolution Reactions

Pandian Ganesan, Moni Prabu, Jakkid Sanetuntikul, and Sangaraju Shanmugam*

Department of Energy Systems and Engineering, Daegu Gyeongbuk Institute of Science and Technology (DGIST), 50-1 Sang-Ri, Hyeongpung-Myeon, Dalseong-gun, Daegu 711-873, Republic of Korea

Supporting Information

ABSTRACT: Electrochemical oxygen evolution and reduction reactions have received great attention due to their importance in several key technologies such as fuel cells, electrolyzers, and metal−air batteries. Here, we present a simple approach to the preparation of cobalt sulfide nanoparticles in situ grown on a nitrogen and sulfur codoped graphene oxide surface. The particle size and phase were controlled by changing the treatment temperature. Cobalt sulfide nanoparticles dispersed on graphene oxide hybrids were successfully prepared by a solid-state thermolysis approach at different temperatures (400, 500, and 600 °C) using cobalt thiourea and graphene oxide. X-ray diffraction studies revealed that hybrids prepared at 400 and 500 °C result in pure CoS_2 phase, whereas the hybrid prepared at 600 °C exhibits Co_9S_8 phase. X-ray photoelectron spectroscopy studies revealed that nitrogen and sulfur simultaneously codoped on the graphene oxide surface, and these sites act to anchor the CoS_2 nanoparticles strongly on the GO surface. The strong coupling between CoS_2 and N,S-GO was reflected in the improvement of the oxygen electrode potential. CoS_2(400)/N,S-GO showed an outstanding oxygen electrode activity with a potential of about 0.82 V against a reversible hydrogen electrode in alkaline medium, which is far better than the performance of precious catalysts such as Pt/C (1.16 V), Ru/C (1.01 V), and Ir/C (0.92 V).

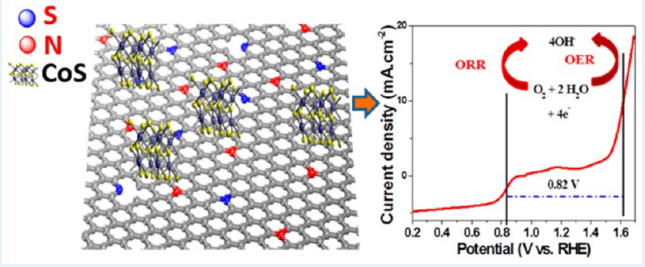

KEYWORDS: *cobalt sulfide, nitrogen and sulfur codoping, oxygen electrode, graphene oxide, water oxidation*

INTRODUCTION

The demand for petroleum resources and issues concerning global warming has made energy storage and conversion devices from renewable fuels the need of the hour. Having high efficiency and environmental benignity, as well as being applicable to portable devices and residential power generation devices such as fuel cells, zinc−air batteries and water electrolysis by polymer electrolyte membrane cells are attractive. The sluggish oxygen electrode kinetics contribute a 15% power loss, which is a critical problem for practical operating fuel cell applications.[1] To address this issue, the development of cost-effective and efficient materials for the oxygen evolution (OER) and oxygen reduction reactions (ORR) are key priorities.[2−6] Presently, composites of the platinum and iridium materials have been brought into use[6−8] to overcome the sluggish oxygen reduction reaction in fuel cells and the sluggish evolution reaction in cathodes used in water electrolysis.[8] The prohibitive cost and scarcity of rarely available materials limit their commercial use.[2]

In order to avoid the use of precious catalysts (Pt, Ir, Ru), various nonprecious materials have been synthesized on the basis of metal nitrogen-doped carbon catalysts and transition metal oxides such as manganese ruthenium composites, CoO_2/MnO_2, Ni_3S_4, among others; these materials have been found to have ORR[8−11] and OER performances similar to those of precious catalysts.[3,12−21] Beyond allowing us to avoid the use of scarce materials, these new catalytic materials are not only efficient but also abundant in the earth. The cobalt sulfides have become robust candidates[3] for use in lithium ion batteries as cathodes with low overpotential, high durability, and good cyclability[22−24] Quantum mechanical calculations have been used to predict the better ORR performance of cobalt sulfide material in acid medium.[25] On the basis of these predictions, recently several cobalt sulfide materials were synthesized, including Co_{1-x} S, Co_3S_4 and Co_9S_8 for ORR[22,23,26] and lithium ion batteries.[27] We have recently reported various metal-doped cobalt oxides (e.g., $CoMn_2O_4$, $NiCo_2O_4$ etc.), all of which have showed good bifunctional activity.[28] Cobalt sulfides doped with nickel, such as $NiCo_2S_4$ and $NiCo_2S_4$@graphene, are also only used as oxygen reduction reaction electrodes.[13,16] Cobalt sulfide nanoparticles supported on graphene have been used as ORR catalysts in alkaline medium.[29,30] In addition, sulfur- and nitrogen-doped carbon and graphene exhibit reasonable ORR activity in alkaline medium.[31,32] The effect of temperature on

Received: October 4, 2014
Revised: May 1, 2015
Published: May 4, 2015

DOI: 10.1021/acscatal.5b00154
ACS Catal. 2015, 5, 3625−3637

the forming of different phases of cobalt sulfides in an open inert atmosphere has been reported.[31,33] Preparation of nanomaterials by solid-state thermolysis has been reported to be a good choice for solution-free synthesis of metal-free and nonprecious ORR electrocatalysts.[17,34−36]

So far, it has been reported that cobalt sulfide (CoS_2) nanoparticles supported on graphene can be used as a catalyst for the ORR; however, the use of such a material has not been investigated for the OER. However, in addition to its ORR activity, the synthesized cobalt sulfide/graphene hybrid has proved to be OER active, with an appreciable minimum overvoltage in alkaline medium. Herein, we introduce a novel and facile synthesis of CoS_2 nanoparticles grown in situ on N, S-doped graphene oxide. This was accomplished by a single-step direct pyrolysis of the GO and cobalt thiourea complex in specially made Swagelok cells (Scheme 1). We, for the first time, have introduced nanosized cobalt sulfide anchored on a nitrogen and sulfur codoped graphene oxide support as a highly efficient oxygen electrode; this material shows better performance compared to those of precious bifunctional catalysts. We developed a scalable and reproducible method for the synthesis of cobalt sulfide, which is anchored on nitrogen and sulfur codoped graphene using solid-state thermolysis processes from earth abundant cobalt complex and graphene oxide.

Scheme 1. Schematic Representation of the Preparation of CoS_2/N,S-GO Hybrid Catalyst by Solid-State Thermolysis Route

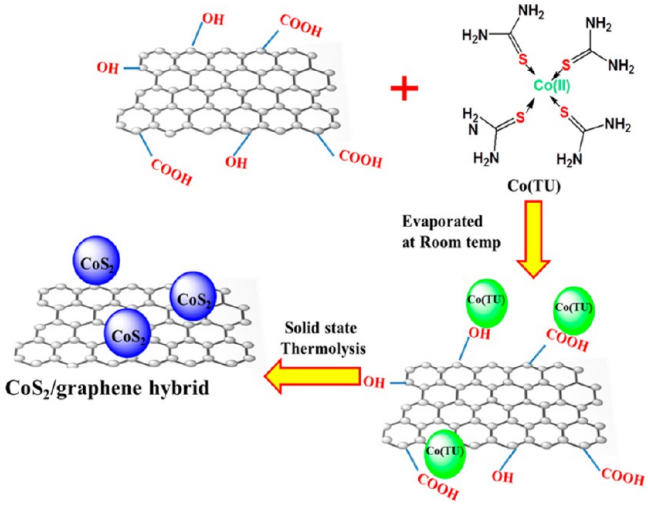

RESULTS AND DISCUSSION

Structural Characterization and Crystallite Size Distribution. Figure 1 shows the crystalline phases of the CoS_2 with space group $Fm\bar{3}m$ (ICSD PDF no. 01-083-0573); these observations were made for the CoS_2(400)/N,S-GO and CoS_2(500)/N,S-GO samples, while the Co_9S_8(600)/N,S-GO sample with the space group $Pa\bar{3}$ (ICSD PDF no. 01-086-2273) was observed for the Co_9S_8(600)/N,S-GO. The crystallite sizes of all catalysts were calculated using the Debye−Scherrer eq 1.

$$D_{hkl} = K\lambda/\beta \mathrm{Cos}\theta \quad (1)$$

where K = 0.1, the dimensionless quantity of shape factor, λ is the X-ray wavelength (λ = 1.5418 Å), β is the full width at half-maximum (fwhm) in rad, and θ is Bragg's angle. On the basis of eq 1, the crystallite size of the CoS_2(400)/N,S-GO and CoS_2(500)/N,S-GO catalysts were calculated and found to be 13.1 and 26.1 nm, respectively. The crystallite size of the Co_9S_8(600)/N,S-GO sample was 42.6 nm. Hence, the above observations show that as the thermolysis temperature increases from 400 to 600 °C, the crystallite size increases, and a dramatic size increment was observed for the catalyst prepared at 600 °C with phase changes to Co_9S_8. The CoS_2(400)/N,S-GO and CoS_2(500)/N,S-GO catalysts exhibit cubic structure with tetrahedral point group having a lattice parameter value of a = 5.539; however, the Co_9S_8(600)/N,S-GO possesses a cubic structures with an octahedral point group a lattice parameter value of a = 9.927. These phase information values reveal the reason for the increment of the crystallite size during the phase changes. Also, in all XRD patterns, a peak at 25°(2 θ) suggests the presence of carbon from the graphene oxide precursor. On the surface of the graphene, except the merger amount of carboxylic group, all functional groups were reduced during heat treatment (Figure S3).

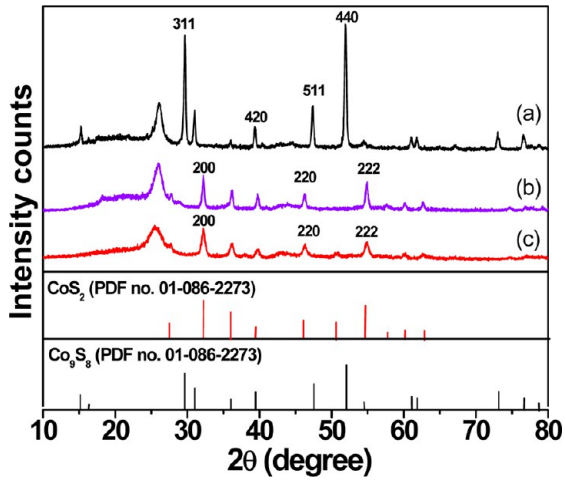

Figure 1. Powder XRD patterns of cobalt sulfide/graphene oxide hybrids (a) Co_9S_8(600)/N,S-GO, (b) CoS_2(500)/N,S-GO, and (c) CoS_2(400)/N,S-GO. The ICSD PDF nos. for CoS_2(400)/N,S-GO, CoS_2(500)/N,S-GO and Co_9S_8(600)/N,S-GO are 01-086-2273, 01-086-2273, and 01-083-0573, respectively.

Figure 2 shows the morphology of CoS_2/graphene oxide composites prepared at 400, 500, and 600 °C. The SEM image of CoS_2(400)/N,S-GO shows that the particles developed on the graphene with an average particle size of about ∼42 nm; however, in the case of CoS_2(500)/N,S-GO, no such development on the graphene oxide surface was observed and there was an average particle size of about ∼67 nm (Figure S1). Co_9S_8(600)/N,S-GO exhibits low particle distribution compared to that of CoS_2(500)/N,S-GO which has an average particle size of about 81 nm. Comparatively, the larger particle size of CoS_2(500)/N,S-GO was due to particle growth that occurred freely; the Co_9S_8(600)/N,S-GO hybrid has a high unit cell parameter value, so it possesses large particle size, which may be due to the high temperature treatment and the fact that the Co_9S_8 particle are highly distributed and agglomerated. Unlike the CoS_2/GO composites, CoS_2 (commercial) and CoS_2(400) samples were found to have particle sizes of 200 nm and particles were aggregated (Figure S2).

In the case of CoS_2(400)/N,S-GO catalyst, CoS_2 particles in situ grown on the surface of the graphene, as indicated by the TEM images (Figure 3a,b), can be clearly seen; hexagonal-shaped CoS_2 particles of various sizes that were projected from

DOI: 10.1021/acscatal.5b00154
ACS Catal. 2015, 5, 3625−3637

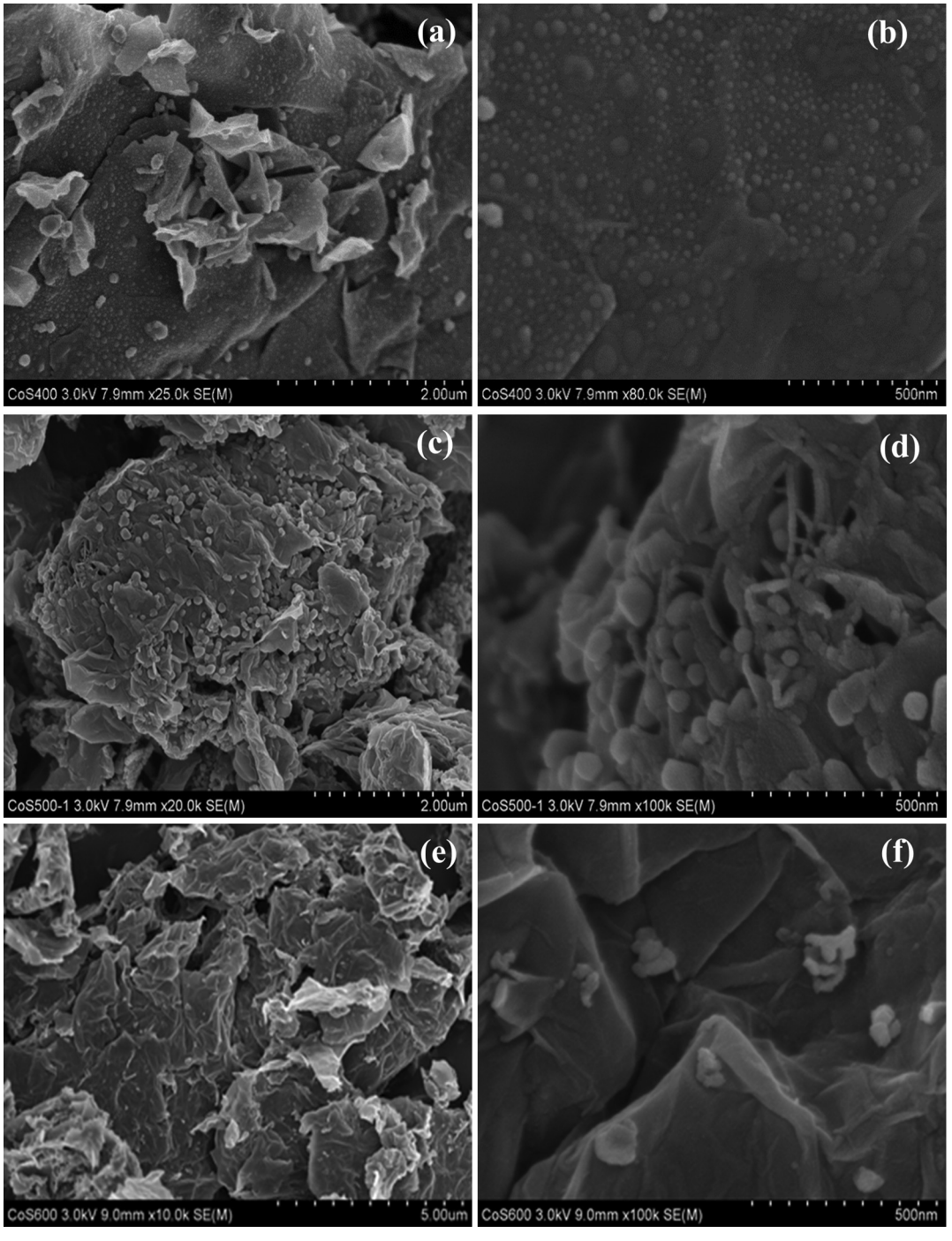

Figure 2. Low- and high-resolution SEM images of (a, b) CoS_2(400)/N,S-GO, (c, d) CoS_2(500)/N,S-GO, and (e, f) Co_9S_8(600)/N,S-GO.

the graphene surface can also be seen, as shown in Figure 3b. The presence of the CoS_2 crystalline lattice fringes with a *d*-spacing value of 0.226 nm corresponds to (211) plane of CoS_2 in the high resolution TEM (Figure 3c) gives additional proof of the particle growth on graphene. TEM elemental mapping of the selected area, in which the particles were grown on graphene surface in CoS_2(400)/N,S-GO, and the corresponding cobalt, sulfur, nitrogen, and carbon mappings are given in Figure 4. It is confirmed that maximum probability of cobalt content is in the particle growth (Figure 4b). However, sulfur is not only present on the CoS_2 particle surface but also present on the surface of the graphene, which has an appreciable amount of sulfur content, and this confirms the existence of sulfur doped in the graphene and confirms the presence of sulfur with cobalt (Figure 4c). Also, in the case of nitrogen mapping, the nitrogen exists almost entirely on the graphene surface, which confirms the existence of nitrogen doping on the graphene surface (Figure 4d).

To confirm the strong coupling between CoS_2 nanoparticles and N,S-doped GO support, we analyzed the band gap of CoS_2 in CoS_2(400)/N,S-GO composite and compared it with that of commercial CoS_2 and synthesized pure CoS_2 nanoparticles. The UV−visible spectra were taken for CoS_2(commercial), CoS_2(400), and CoS_2(400)/N,S-GO from the reflectance spectra, which show CoS_2 peaks at 332 nm for CoS_2(commercial), 335 nm for CoS_2(400), and at 346 nm for

DOI: 10.1021/acscatal.5b00154
ACS Catal. 2015, 5, 3625−3637

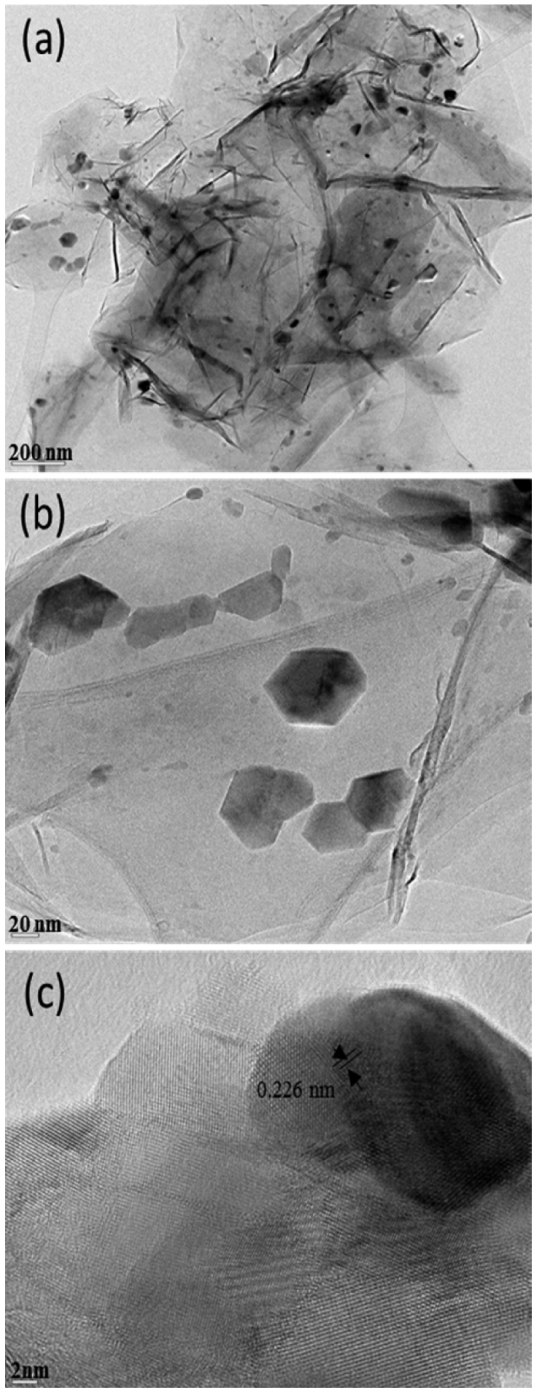

Figure 3. TEM images of CoS_2(400)/N,S-GO at (a) low and (b) high magnifications. (c) High-resolution TEM image shows the lattice fringes of CoS_2(400)/N,S-GO.

CoS_2(400)/N,S-GO (Figure 5). Moreover, CoS_2(400)/N,S-GO can be seen to have a surface-adsorbed graphene oxide peak at 288 nm. Among the three catalysts, the CoS_2(400)/GO exhibits a red shift in wavelength, indicating a change in the electronic band gap level. In order to understand the band gap of the three catalysts, the Kubelka–Munk function was used to calculate the band gap of CoS_2(400)/N,S-GO using eq 2[40,41]

$$F(R) = \alpha/S = (1 - R)^2/(2R) \quad (2)$$

where α is the absorption coefficient, S is the scattering coefficient, and R is the reflectance. The corresponding band gaps for the CoS_2(commercial), CoS_2(400), and CoS_2(400)/N,S-GO are 3.50, 3.41, and 3.25 eV, respectively[40,42](Figure 5b,d,f). The decrement of the band gap of the CoS_2(400) and CoS_2(commercial) compared to that of the CoS_2(400)/N,S-GO, might be due to composite effect of GO and particle agglomeration, which is also obvious from the SEM images of the CoS_2(400) and CoS_2(commercial) samples (Figure S2). The decrease in the CoS_2 edge band gap of the hybrid CoS_2(400)/N,S-GO compared to that of the CoS_2(400) and CoS_2(commercial) is due to the in situ development of CoS_2 nanoparticles on the graphene oxide surface. Because of the low band gap, unlike the CoS_2(400) and CoS_2(commercial), the CoS_2(400)/N,S-GO hybrid shows better oxygen reduction and oxygen evolution properties.

The XPS survey spectrum of the CoS_2(400)/N,S-GO composite is presented in Figure 6a. The peak (S_{2p}) at 163.4 eV corresponds to polymeric S_n^{2-}.[24] The peak at 163.8 eV explains the sulfur bonded with carbon (−C−S-C−), which explains the presence of sulfur doping in graphene (Figure 6b); this trend in sulfur bonding with carbon also stands as direct evidence for the observations performed in the TEM mapping (Figure 4e).[43] The presence of the peak at 164.6 eV strongly suggests the presence of nitrogen and sulfur incorporated on the graphene.[44] The existence of a polymeric sulfur (S_n^{2-}) group can be beneficial in anchoring the cobalt sulfide nanoparticles on the graphene surface (Figure 6b). Moreover, Co_{2p} peaks for Co−S at 779.3 and 781.3 eV confirm the existence of a Co−S bond of the CoS_2 formation; the peaks at 782.3 and 786.0 eV are due to Co−S with surface-adsorbed hydroxide species[24,45] (Figure 6c). The N_{1s} peaks observed at 398.6, 399.8, and 401.7 eV are attributed to the presence of the pyridinic-, pyrrolic-, and graphitic-type nitrogen functional groups in graphene surface, respectively[46] (Figure 6d). This provides additional evidence that nitrogen is doped on the graphene surface. The XPS results strongly complement the STEM nitrogen mapping results (Figure 4d). The C_{1s} spectra support the idea of more sp^2 nature of the carbon, which was confirmed by the peak at 284.5 eV with high intensity and the sp^3 peak at 285.6 eV with low intensity (Figure 6e). Exceptionally, sulfur, in CoS_2(500)/N,S-GO, also followed the same XPS trends (Figure S4). There was a difference in the bonding nature of sulfur that can be inferred from the XP spectra for CoS_2(400)/N,S-GO and CoS_2(500)/N,S-GO (Figure 6f). As mentioned above, unlike the CoS_2(500)/N,S-GO catalyst, the CoS_2(400)/N,S-GO sample showed a polymeric S_n^{2-} peak at 163.4 eV, but CoS_2(500)/N,S-GO exhibits a dimeric S_2^{2-} peak at 162.6 eV. This is direct proof of the presence of CoS_2, which is in-built through the polysulfide chain in CoS_2(400)/N,S-GO (Figure 6f).

Figure 7a shows the FT-IR spectra of the CoS_2(400)/N,S-GO, CoS_2(commercial) and CoS_2(400) catalysts. For all the catalysts, the peak observed at 452 cm^{-1} confirms the presence of Co−S bond,[47,48] and the presence of polysulfide group frequencies within the range 450−500 cm^{-1}[49] were only observed for CoS_2(400)N,S-GO and CoS_2(400) samples that were prepared from the cobalt thiourea precursor by solid-state thermolysis. The peak observed at 471 cm^{-1} was attributed to polysulfide for the CoS_2(400)/N,S-GO sample alone. This observation was further supported by the XPS results, which showed polysulfide peak at 163.4 eV for CoS_2(400)/N,S-GO and CoS_2(500)/N,S-GO. Moreover, there was a difference in wavenumber for the polysulfide peaks between CoS_2(400)/N,S-GO (471 cm^{-1}) and CoS_2(400) (466 cm^{-1}). According to

DOI: 10.1021/acscatal.5b00154
ACS Catal. 2015, 5, 3625−3637

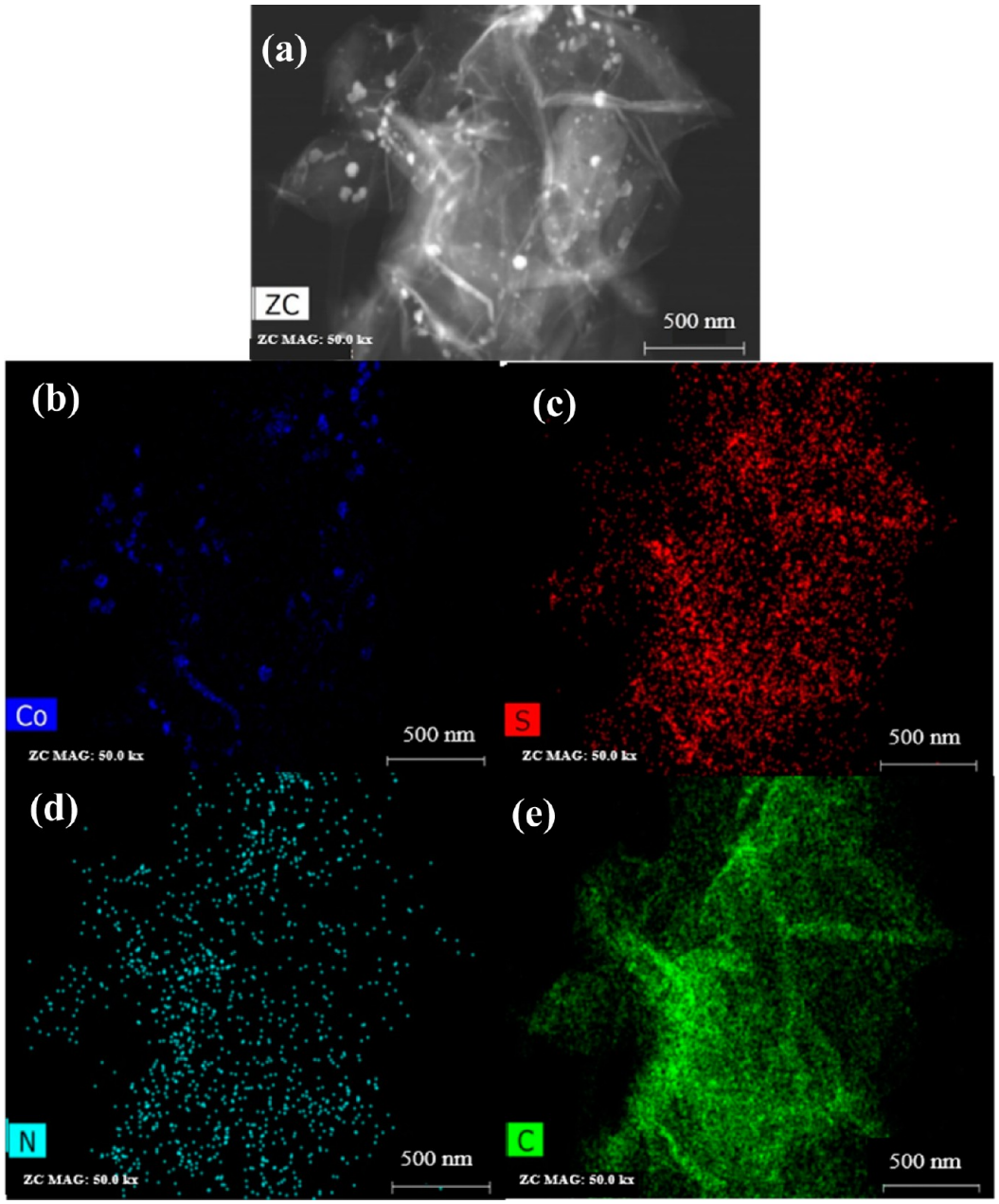

Figure 4. TEM elemental mapping analysis of CoS_2(400)/N,S-GO. (a) Selected area and corresponding elemental mappings for (b) cobalt, (c) sulfur, (d) nitrogen, and (e) carbon.

Hook's law, the increment of the wavenumber of the CoS_2(400)/N,S-GO sample may be due to the strong bonding of polysulfide with graphene; the same peak for the CoS_2(400) sample was observed at a higher wavelength (466 cm^{-1}), representing weak bonding due to low carbon content from the precursor. Further, unlike the CoS_2(commercial) sample, CoS_2(400)/N,S-GO shows characteristic C-$(S-S)_n$ peaks at 508 and 521 cm^{-1}. The same characteristic peak also appears for the CoS_2(400) at 466 cm^{-1} with low intensity, which may be due to the low carbon content. The presence of the C-$(S-S)_n$ bond was also further confirmed by the Raman spectroscopy (Figure 7b), which shows a peak at 665 cm^{-1}.[49] The IR, Raman, and XPS results suggest that the CoS_2 nanoparticles are strongly coupled with the graphene surface and its coupling could be responsible for the better bifunctional activity.

The amounts of carbon, nitrogen, and sulfur were measured by CHNS (carbon, hydrogen, nitrogen, and sulfur) elemental analysis; the results are listed in Table 1. The carbon content values for the CoS_2(400)/N,S-GO, CoS_2(500)/N,S-GO, and Co_9S_8(600)/N,S-GO samples were 61.8, 61.2, and 52.1 wt %, respectively; sulfur content in the CoS_2(400)/N,S-GO, CoS_2(500)/N,S-GO, and Co_9S_8(600)/N,S-GO catalysts were 14.3, 14.5, and 11.9 wt %, respectively, which shows that as the temperature increases, the sulfur content decreases. Also, the nitrogen contents in the CoS_2(400)/GO, CoS_2(500)/N,S-GO, and Co_9S_8(600)/N,S-GO were 3.9, 3.5, and 4.6 wt %, respectively. BET (Brunauer–Emmett–Teller) specific surface area measurements show pore diameters of up to 0–5 nm for the CoS_2(400)/N,S-GO, CoS_2(500)/N,S-GO, and Co_9S_8(600)/N, S-GO samples; however, the CoS_2(400)/N,S-GO sample had a slightly smaller pore size compared to that of

DOI: 10.1021/acscatal.5b00154
ACS Catal. 2015, 5, 3625–3637

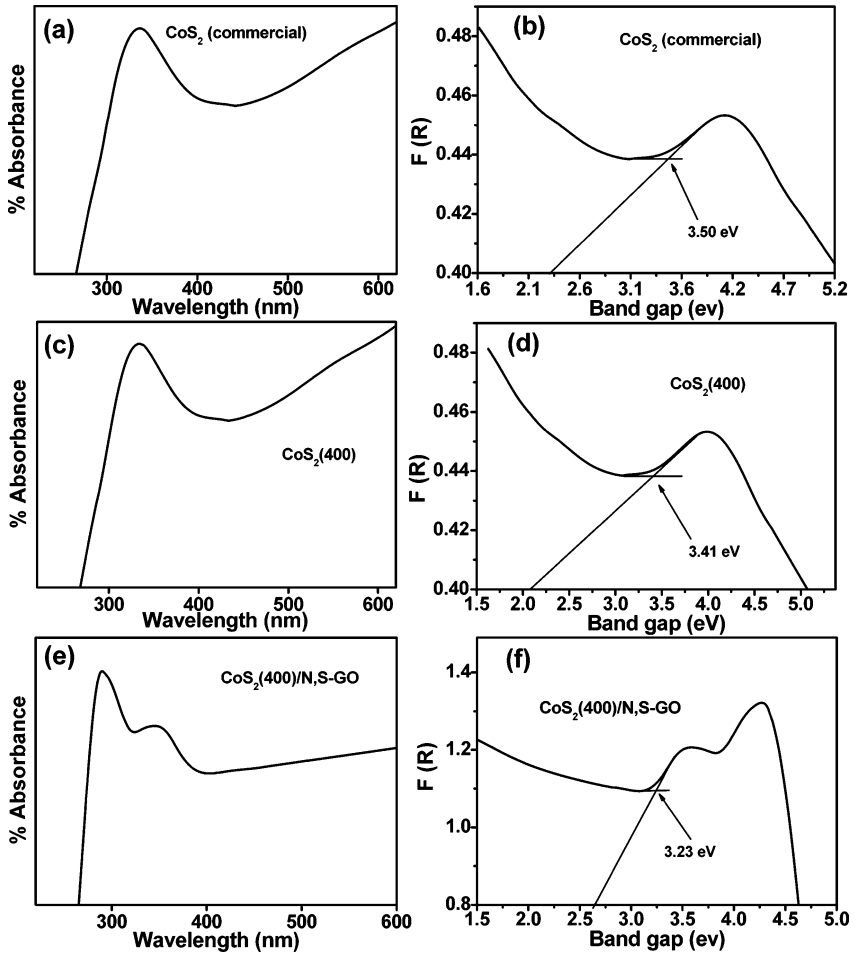

Figure 5. UV−visible spectra of (a) CoS_2 (commercial), (c) $CoS_2(400)$, and (e) $CoS_2(400)$/N,S-GO and (b, d, f) its corresponding band gap plots using Kubelka−Munk functions.

the $CoS_2(500)$/N,S-GO sample. The surface area of $CoS_2(400)$/N,S-GO, $CoS_2(500)$/N,S-GO, and $Co_9S_8(600)$/N,S-GO samples were found to be about 19, 10, and 13 m^2 g^{-1}, respectively (Figure 8). The corresponding pore size distributions (insets in Figure 8) of $CoS_2(400)$/N,S-GO, $CoS_2(500)$/ N,S-GO, and $Co_9S_8(600)$/N,S-GO show mesopores with almost the same average sizes of about 3.5, 2.7, and 2.5 nm. The liquid N_2 adsorption and desorption isotherms show the approximate surface area for the $CoS_2(400)$/N,S-GO, $CoS_2(500)$/N,S-GO, and $Co_9S_8(600)$/N,S-GO samples, but the $CoS_2(400)$/N,S-GO sample shows a slightly better surface area because it possesses CoS_2 development on the surface of reduced graphene oxide. Hence, there were differences in BET surface areas among the three samples, even though the average pore size distribution was almost the same for all samples, because strong interaction between CoS_2 and N,S-GO was the key factor for better bifunctional behavior (Table 2).

Electrochemical Characterization. Cyclic voltammetry measurement was carried out for each sample at a scan rate of 10 mVs^{-1} in both Ar-saturated atmosphere for background correction and O_2-saturated 0.1 M KOH aqueous solution. Furthermore, the current densities for all the electrochemical behavior were calculated based on the geometrical surface area (GSA) of the electrode (0.071 cm^{-2}). When we investigated the electrocatalytic behavior with a 0.25 mg cm^{-2} catalyst coating, the onset potentials at 70 μA from RDE studies for the $CoS_2(400)$/N,S-GO, $CoS_2(500)$/ N,S-GO, and $Co_9S_8(600)$/N,S-GO are 0.97, 0.97, and 0.95 V, respectively (Figure 9, Figure S5, Table 3). The ORR $E_{1/2}$ for the $CoS_2(400)$/N,S-GO catalyst is 40 mV higher than that of the $Co_9S_8(600)$/N,S-GO catalyst. Moreover, the rotating disc electrode (RDE) polarization curves at various rotations showed an improved diffusion limited current. The insets in Figure 9b−d show the corresponding K−L plots, which were plotted using the inverse of rotation ($\omega^{-1/2}$) versus the inverse of current density (J^{-1}); the plots show good linearity for the $CoS_2(400)$/N,S-GO, $CoS_2(500)$/N,S-GO, and $Co_9S_8(600)$/N,S-GO samples (Figure 9b−d). The ORR electron transfer numbers were calculated from K−L plots for the $CoS_2(400)$/N,S-GO, $CoS_2(500)$/N,S-GO, and $Co_9S_8(600)$/N,S-GO samples are 3.81, 3.87, and 3.85, respectively. The half-wave potential ($E_{(1/2)}$) observed at 3 $mAcm^{-2}$ for $CoS_2(400)$/N,S-GO, $CoS_2(500)$/N,S-GO, and $Co_9S_8(600)$/N,S-GO samples were 0.79, 0.76, and 0.75 V against RHE, respectively (Figure 10a, Table 3). The $CoS_2(400)$/N,S-GO composite showed a 30 mV positive shift compared to that of the $CoS_2(500)$/N,S-GO and a shift of about 40 mV when compared to that of the $Co_9S_8(600)$/N,S-GO sample. The $E_{1/2}$ of $CoS_2(400)$/N,S-GO (physical mixture (phy. mix)) shows 90 mV lower than hybrid catalyst, which demonstrate the strong coupling between CoS_2 nanoparticles and N,S-GO support prepared in situ. To understand the OER behavior, linear sweep voltammetry was carried out between 0.0 and 1.7 V against RHE at 1600 rpm in RDE at a scan rate of 10 mV s^{-1} (Figure 10b). At 10 mA cm^{-2},

DOI: 10.1021/acscatal.5b00154
ACS Catal. 2015, 5, 3625−3637

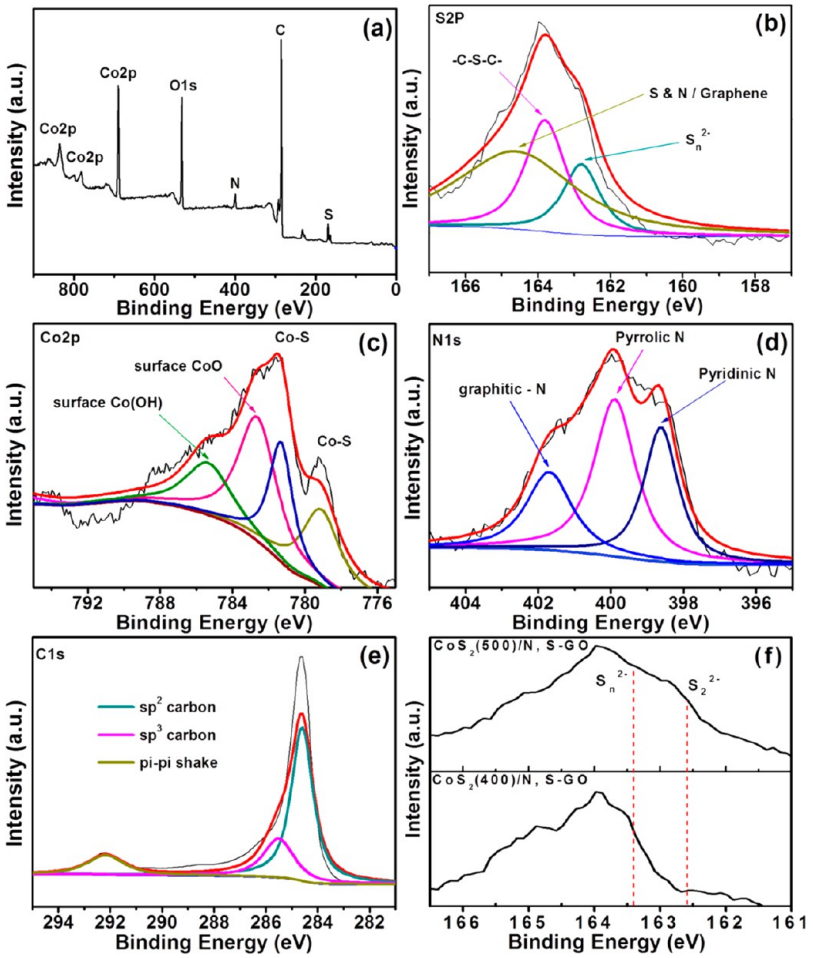

Figure 6. (a) XPS survey scan of $CoS_2(400)$/N,S-GO, (b, c, d, and e) S 2p, Co 2p, N 1s, and C 1s XP spectrum of $CoS_2(400)$/N,S-GO, respectively, (f) S 2p peak shift from S_n^{2-} to S_2^{2-} between $CoS_2(400)$/N,S-GO and $CoS_2(500)$/N,S-GO.

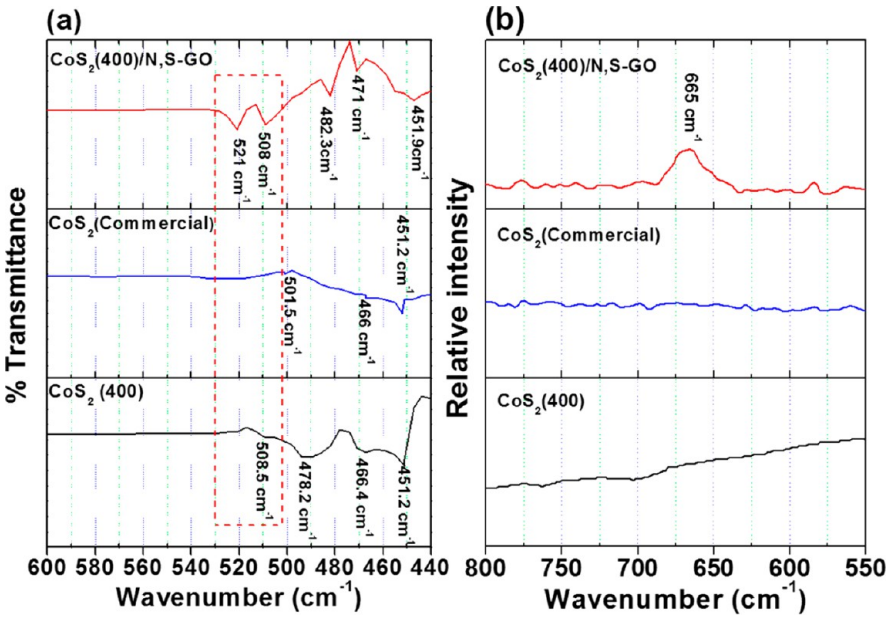

Figure 7. (a) FT-IR and (b) Raman spectra of CoS_2 (400), CoS_2 (commercial), and $CoS_2(400)$/N,S-GO.

the OER potential for the $CoS_2(400)$/N,S-GO, $CoS_2(500)$/N,S-GO, and $Co_9S_8(600)$/N,S-GO) samples were 1.61, 1.62, and 1.63 V versus RHE, respectively (Table 3). The oxygen electrode potentials (Figure 10c), calculated using the solar to fuel device conversion scale[50] of $\Delta E_{1/2}$= (OER at 10 − ORR at 3 mAcm $^{-2}$) were found to be 0.82, 0.86, and 0.88 V against

DOI: 10.1021/acscatal.5b00154
ACS Catal. 2015, 5, 3625−3637

Table 1. CHNS Elemental Analysis of CoS_2(400)/N,S-GO, CoS_2(500)/N,S-GO, and Co_8S_9(600)/N,S-GO

	composition (wt %)		
sample	sulfur	nitrogen	carbon
CoS_2(400)/N,S-GO	14.3	3.9	61.8
CoS_2(500)/N,S-GO	14.5	3.5	61.2
Co_8S_9(600)/N,S-GO	11.9	4.6	52.1

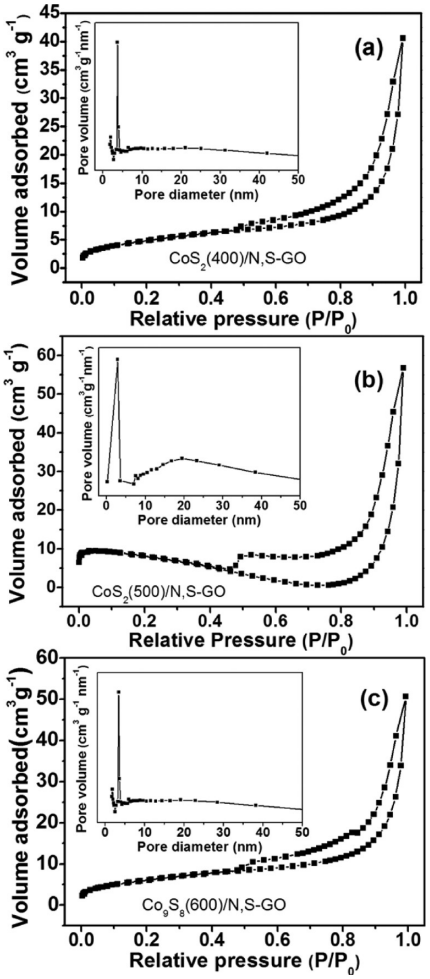

Figure 8. BET adsorption−desorption studies and pore size distributions (inset) of (a) CoS_2(400)/N,S-GO, (b) CoS_2 (500)/N,S-GO, and (c) Co_9S_8(600)/N,S-GO.

Table 2. Comparison of BET Specific Surface Area and Pore Size Distributions of CoS_2(400)/N,S-GO, CoS_2(500)/N,S-GO, and Co_9S_8 (600)/N,S-GO Catalysts

sample	BET surface area(m^2g^{-1})	average pore size (nm)
CoS_2(400)/N,S-GO	19	3.5
CoS_2(500)/N,S-GO	10	2.7
Co_9S_8(600)/N,S-GO	13	2.5

RHE for CoS_2(400)/N,S-GO, CoS_2(500)/N,S-GO, and Co_9S_8(600)/N,S-GO samples, respectively. Among the three catalysts, the CoS_2(400)/N,S-GO catalyst showed better bifunctional activity due to the development of particles of CoS_2 on the graphene surface. Also, the bifunctional activity is due to cobalt sulfides and N,S-codoped graphene, which favors better electronic movement. This is clear from Figure 10a,b, in which it can be seen that without CoS_2 particles, N,S-GO sample shows very low levels of ORR and OER activity. Further, the mass activities for both ORR and OER give additional proof that CoS_2(400)/N,S-GO has better bifunctional activity (Figure 11). The ORR mass activity for CoS_2(400)/N,S-GO, CoS_2(500)/N,S-GO, and Co_9S_8(600)/N,S-GO samples at 0.85 V are 1.21, 0.32, and 0.12 mA mg^{-1}, respectively. The mass activity of CoS_2(400)/N,S-GO catalyst was 1 order magnitude higher than Co_9S_8(600)/N,S-GO and 4-fold higher than CoS_2(500)/N,S-GO catalysts, indicating a strong coupling between CoS_2 nanoparticles to the surface of graphene oxide.

Overall, as the temperature increases from 400 to 600 °C, the ORR performance decreased, as shown in Figure 10. The decreased activity of catalysts prepared at higher temperature (CoS_2(500)/N,S-GO and Co_9S_8(600)/N,S-GO) can be attributed to the increased particles size and also due to breaking of polymeric sulfur bonds between CoS_2 and N,S-GO support, which leads to the particles agglomeration. This reflects in increased particle size and their board size distribution of the catalysts prepared at 500 and 600 °C (Figure S1). Further, as far as CoS_2(600)/N,S-GO catalyst concerned, the particles were severely agglomerated, forming larger particles with an average particle size of 81 nm with a broad particle distribution (Figure S1).[51−53] It should be also noted that the phase of cobalt sulfide is different between the catalysts prepared at 400 and 600 °C. The catalyst prepared at 400 °C showed high activity among the prepared catalysts and can be attributed to the smaller size narrow size dispersion, strong-coupling effect between the CoS_2 and N,S-GO surface. The OER mass activity at 1.62 V for CoS_2(400)/N,S-GO, CoS_2(500)/N,S-GO, and Co_9S_8(600)/N,S-GO are 37.1, 36.9, and 26.2 mA mg^{-1}, respectively. Moreover, the ORR Tafel slopes, calculated for CoS_2(400)/N,S-GO, CoS_2(500)/N,S-GO, and Co_9S_8(600)/N,S-GO samples are 30, 29, and 47 mV/decade, respectively; the OER Tafel slopes calculated for CoS_2(400)/N,S-GO, CoS_2(500)/N,S-GO, and Co_9S_8(600)/N,S-GO samples are 75, 80, and 96 mV/decade, respectively. The Tafel slopes for the both ORR and OER are in the order of CoS_2(400)/N,S-G < CoS_2(500)/N,S-GO < Co_9S_8(600)/N,S-GO. The CoS_2(400)/N,S-GO catalyst exhibited lower overpotential compared to CoS_2(500)/N,S-GO and Co_9S_8(600)/N,S-GO catalysts. The lower Tafel slopes observed for CoS_2(400)/N,S-GO and CoS_2(500)/N,S-GO catalysts suggest an improved ORR activity and follows the direct four-electron transfer mechanism as proposed by Fang et al. and Damjanovic et al.[54,55] All three GO supported cobalt sulfide catalysts exhibit lower Tafel slopes value for ORR at the overpotential regions of 0.80 to 1.0 V for ORR and 1.4 to 1.8 V for OER, suggests the same reaction pathway and rate-determining steps observed for these catalysts, which is consistent with the Co-based nonprecious catalysts.[56,57] From Figure 11, it is clear that the intrinsic surface property of CoS_2(400)/N,S-GO makes better activity compared to CoS_2(500)/N,S-GO and CoS_2(500)/N,S-GO. Also, the extent of incomplete oxygen reduction for CoS_2(500)/N,S-GO and Co_8S_9(600)/N,S-GO is responsible for their low mass activity. This result also suggests the change of crystalline phase from CoS_2 to Co_9S_8 does not affect the reaction pathway, but it can alter the rate of ORR catalytic reaction. The ratio of carbon to CoS_2 for the CoS_2(400)/N,S-GO is about 3:2, which provides facile electron movement for the oxygen electrode; also, CoS_2(400)/N,S-GO has a slightly higher BET surface area (19 m^2 g^{-1}) than that of CoS_2(500)/

DOI: 10.1021/acscatal.5b00154
ACS Catal. 2015, 5, 3625−3637

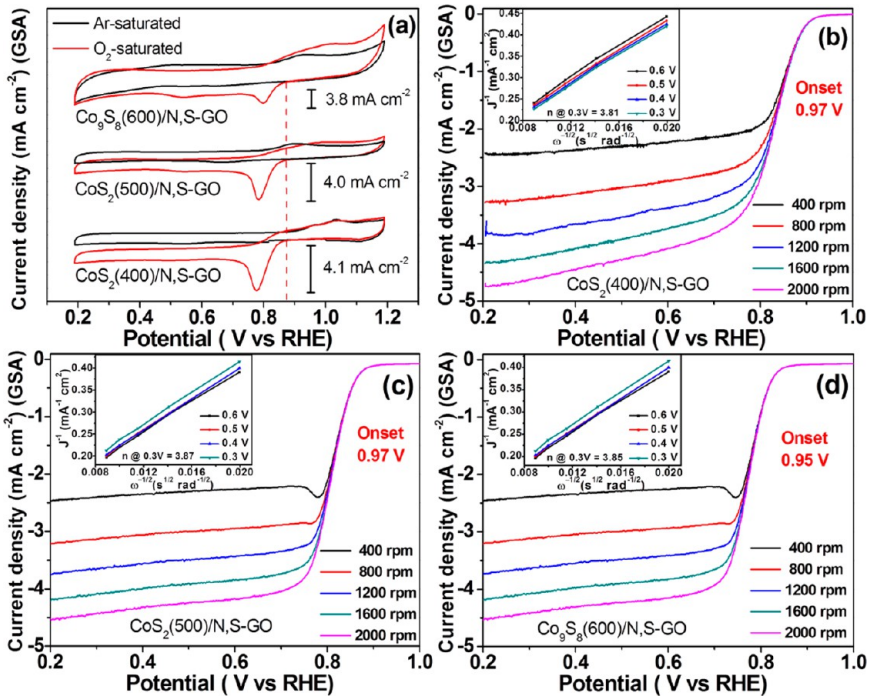

Figure 9. (a) CV and RDE curves at various rpm and insets show K–L plots of (b) CoS_2(400)/N,S-GO, (c) CoS_2(500)/N,S-GO, and (d) Co_9S_8(600)/N,S-GO catalysts. GSA – Geometrical surface area.

Table 3. Comparison of Electrochemical Performance of CoS_2/N,S-GO with Various Precious and Non-Precious Catalysts Reported in the Literature[a]

catalysts	catalyst loading (mg cm^{-2})	ORR onset potential vs RHE (V)	OER potential at I = 10 mA cm^{-2} vs RHE (V)	ORR potential at I = −3 mA cm^{-2} vs RHE (V)	oxygen electrode ΔE = (OER−ORR) vs RHE (V)
CoS_2(400)/N,S-GO	0.25	0.97	1.61	0.79	0.82
CoS_2(500)/N,S-GO	0.25	0.97	1.62	0.76	0.86
Co_9S_8(600)/N,S-GO	0.25	0.95	1.63	0.75	0.88
IrO_2	0.25	-	1.61	-	-
20 wt % Pt–Ru/C	0.25	-	1.62	0.74	0.88
20 wt % Pt/C	0.25	-	2.02	0.86	1.16
Mn-Oxide[51]	0.50	-	1.77	0.73	1.04
$NiCo_2O_4$[52]	0.50	0.94	1.62	0.78	0.84
Fe–N_x/C/L58SCF[55]	0.24	0.82[b]	1.80	0.71	1.09

[a]The ORR and OER activity of precious catalysts (20% Pt/C, 20% Pt–Ru/C and IrO_2) were obtained from RDE at various rotations and K–L plots from Figure S6. [b]The onset potential for Fe-Nx/C/L58SCF was calculated at the current density of −1 $mAcm^{-2}$.

N,S-GO (10 m^2 g^{-1}). The oxygen electrode potentials of CoS_2(400)/N,S-GO sample was compared with several control samples such as CoS_2(500)/N,S-GO, Co_9S_8(600)/N,S-GO and that of CoS_2 prepared by solid-state thermolysis and physical mixture of CoS_2 with graphene CoS_2(400)/Gr (phy. mix) and CoS_2/N,S-GO (phy. mix). This comparison clearly explains the role of graphene oxide during synthesis: it facilitates a better electron transfer rate (Figure S6). This behavior also explains the effect of nitrogen- and sulfur-doped graphene oxide, which are involved in enhancing the bifunctional behavior. Even though CoS_2(400)/N,S-GO and CoS_2(500)/N,S-GO had the same crystallographic phases, the better bifunctional behavior of CoS_2(400)/N,S-GO compared to that of CoS_2(500)/N,S-GO may be due to the anchoring of CoS_2 on GO through polysulfide bonding, as observed by XPS, FT-IR, and Raman results. The oxygen electrode potential of the CoS_2(400)/N,S-GO sample is 0.82 V vs RHE, which is an outstanding performance compared to that of the precious catalysts such as 20% Pt/C, 20% Pt–Ru/C(0.88 V) and IrO_2 and nonprecious catalysts like MnO_2/NCNT(~0.90 V), $NiCo_2O_4$(0.84 V) and even recently reported nonprecious bifunctional catalyst Fe-Nx/C/L58SCF (Table 3).[58−60] The ORR kinetic current density (J_k) for CoS_2(400)/N,S-GO obtained from the K–L plot (Figure S7) is compared with the precious catalysts, which is showing comparable activity with 20% Pt/C (7.7 mA.cm^{-2}) and better compared to the rest of the reported precious catalysts and nonprecious catalysts (Table S1).[60−64] The ORR $E_{1/2}$ potential of CoS_2(400)/N,S-GO (0.79 V) catalyst is 50 mV higher than precious Pt–Ru/C (0.74 V) and 180 mV higher than IrO_2 (0.61 V) catalyst. However, the $E_{1/2}$ of CoS_2(400)/N,S-GO is 70 mV lower than the state-of-the-art, Pt/C (0.86 V) catalyst. Even though the ORR performance is lower than Pt/C catalyst, if we consider the cost and availability of platinum, then our CoS_2(400)/N,S-GO exhibits several advantages such as cost and earth abundance (Figure S7). Pt–Ru/C- and IrO_2-based catalysts exhibited skewed ORR RDE traces with disturbed diffusion-limited current, which may be

DOI: 10.1021/acscatal.5b00154
ACS Catal. 2015, 5, 3625−3637

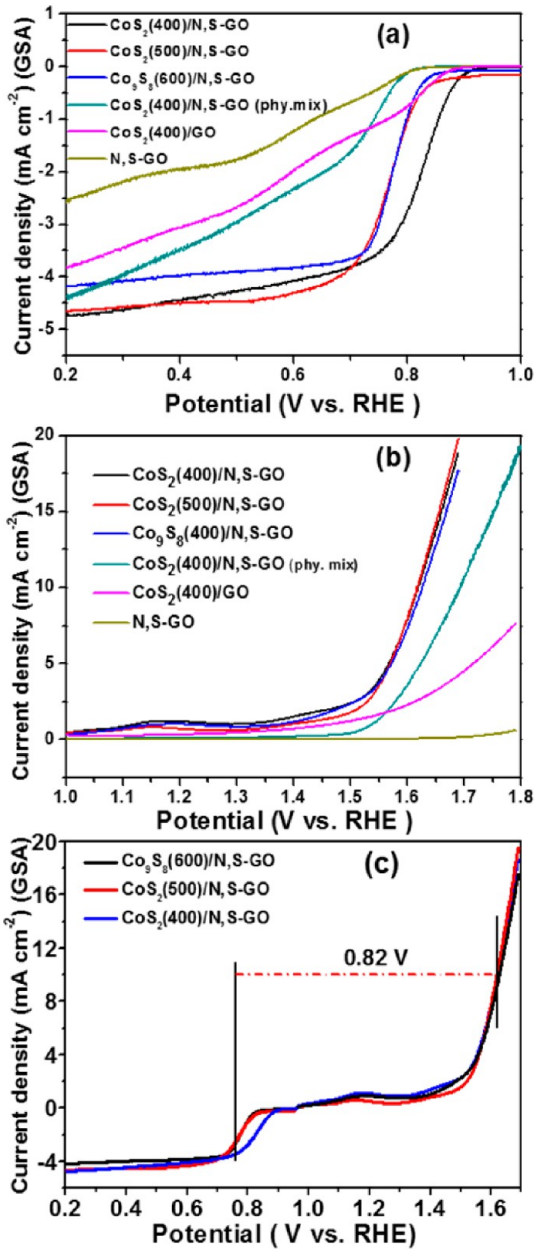

Figure 10. Comparative (a) ORR and (b) OER activities of $CoS_2(400)$/N,S-GO, $CoS_2(500)$/N,S-GO, $Co_8S_9(600)$/N,S-GO, $CoS_2(400)$/N,S-GO (phy. mix), N,S-GO and $CoS_2(400)$/GO (c) oxygen electrode performance of the $CoS_2(400)$/N,S-GO, $CoS_2(500)$/N,S-GO, and $Co_8S_9(600)$/N,S-GO at 1600 rpm in 0.1 M KOH with a scan rate of 10 mV s^{-1}.

due to the nature of the samples. This observation indicates the poor activity of these catalysts for ORR (Figure S7).

The electrode stability was carried out for both ORR and OER activity to understand the durability of bifunctionality. The durability for the oxygen reduction reaction was examined by performing repeated potentio-dynamic cycling for 5000 cycles with a potential range of 0.2 to 1.0 vs RHE at a scan rate of 50 mVs^{-1} in an O_2-saturated atmosphere. After 3000 and 5000 cycles, the $E_{1/2}$ of CoS_2 (400)/N, S-GO catalyst showed a loss ($E_{1/2}$) of about 30 and 50 mV, respectively (Figure S8a). The gradual decay of the performance of CoS_2 (400)/N,S-GO catalyst after 3000 and 5000 potentio-dynamic cycling can be attributed to the breaking of polysulfide linkage between particles and support, leads to the CoS_2 particle agglomeration, which may responsible for the decrement in half-wave potential. Further, we also evaluated the OER electrode stability by repeated LSVs in a potential range of 0.9 to 1.8 V vs RHE and monitored the overpotential change at a current density value of 10 mA cm^{-2} (Figure S8b). The OER overpotential values for fresh, 35th, and 100 cycled electrodes were found to be 1.62, 1.64, and 1.67 V, respectively, suggesting a small potential loss until 100 cycles. These results indicated that the surface property of the $CoS_2(400)$/N,S-GO catalyst was still maintained during the potential cycling stability test. During the OER stability test, a large amount of oxygen gas was evolved from the electrode surface, and the electrode layer was peeled off from the surface of glassy carbon, which prevents the continuation of the stability test. The improvement of the electrode stability is now under investigation, and the results will be reported in our future studies.

CONCLUSION

A cobalt sulfide/N,S-graphene oxide hybrid catalyst using solid-state thermolysis at various temperatures was successfully prepared from cobalt thiourea complex and graphene oxide precursors. We found that the cobalt sulfide/graphene oxide hybrid material also involves excellent oxygen evolution reaction. Among the composite samples, the hybrid $CoS_2(400)$/N,S-GO exhibits good bifunctional activity of about 0.82 V in alkaline medium with remarkable and robust oxygen evolution and oxygen reduction reaction of about 1.62 and 0.79 V vs RHE, respectively. This excellent performance was due to the spherical development of CoS_2 on the graphene and anchoring of CoS_2 on the graphene. XPS, FT-IR, Raman, SEM and TEM micrographs interpretations also support the incorporation of cobalt sulfides on the graphene through polysulfide bonding.

METHODS

Synthesis of CoS_2/Graphene. About 200 mg of graphene oxide was mixed with 7 mL of acetone, and the solution was sonicated until it completely dispersed. Then, about 0.15 g of cobalt thiourea complex (Supporting Information), $Co(TU)_4(NO_3)_2$ was added to the mixture and stirred at 35 °C until all the solvent was evaporated. Then, the dried solid was ground well and loaded into a Swagelok union cell. The cell was heated to 400 °C for 2 h a heating rate of 5 °C/min. After cooling to room temperature, the Swagelok cell was carefully opened, and the product was collected for further characterization. The catalysts prepared at 400, 500, and 600 °C, were denoted $CoS_2(400)$/N,S-GO, $CoS_2(500)$/N,S-GO, and $Co_9S_8(600)$/N,S-GO, respectively. During the solid-state thermolysis under autogenic pressure, the heteroatoms were doped on the graphene oxide surface, and there was a simultaneous formation of CoS_2 nanoparticles. The same preparation procedure was also followed to prepare $CoS_2(400)$ without graphene oxide: the cobalt thiourea complex was heated to 400 °C (CoS_2). In addition, the same preparation procedure was also followed to prepare N,S-GO without cobalt thiourea: the graphene oxide and thiourea was taken in the ratio 3:2 and heated to 400 °C. To prepare CoS_2/N,S-GO physical mixture by a two-step method, Cobalt thiourea and graphene oxide were prepared separately at 400 °C using Swagelok cells. Then, prepared N,S-GO and $CoS_2(400)$ were mixed with a ratio of 3:2 using 7 mL of acetone and stirred the contents until

DOI: 10.1021/acscatal.5b00154
ACS Catal. 2015, 5, 3625−3637

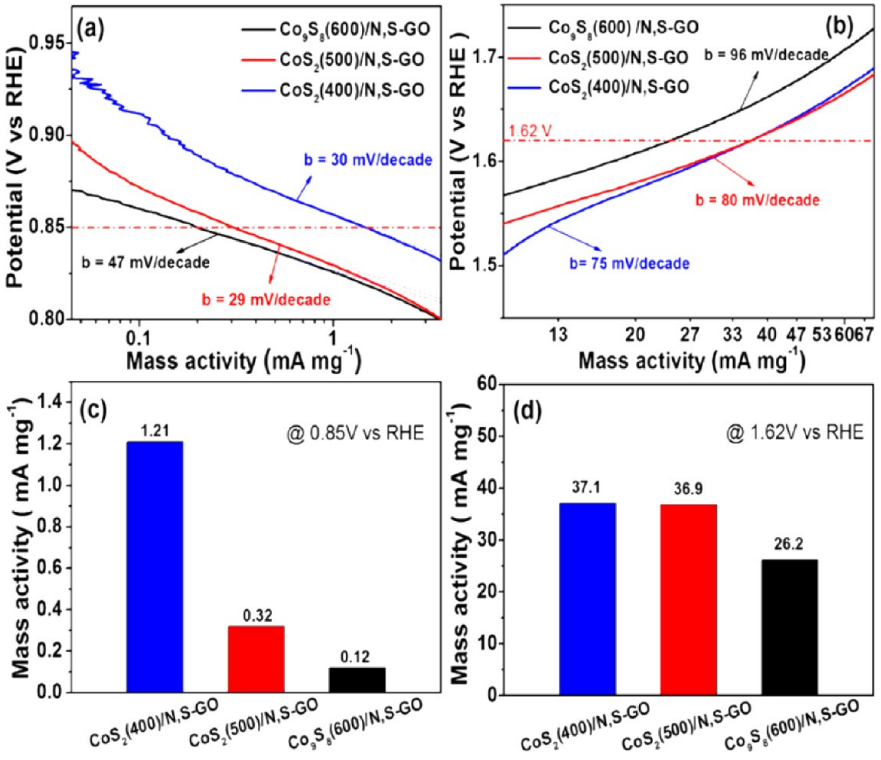

Figure 11. Tafel plots of (a) ORR and (b) OER for CoS_2(400)/N,S-GO, CoS_2(500)/N,S-GO, and Co_9S_8(600)/N,S-GO catalysts and corresponding (c) ORR, and (d) OER mass activity histograms.

all the solvent evaporated, which is labeled as CoS_2(400)/N,S-GO (phy. mix), and a physical mixture of CoS_2 and GO (without N,S-doping) was also used for the comparison (Scheme 1).[37]

Material Characterizations. The heat-treated Co-$(TU)_4(NO_3)_2$ with graphene oxide was characterized using XRD for phase confirmation, UV−vis spectroscopy (Agilent Cary-5000) to determine the electronic properties, and FT-IR Nicolt iS10 (Thermo Scientific) and Raman spectra, Thermo Nicolet ALMEGA XR (Thermo Scientific) were used to determine the interaction of cobalt sulfides particles with graphene. X-ray diffraction (XRD) measurements were carried out using an X-ray diffractometer (Rigaku, MiniFlex 600) with a copper anode of Kα radiation (1.5418 Å). To understand the elemental composition, CHNS (carbon, hydrogen, nitrogen and sulfur) elemental analysis was carried out using an elemental analyzer (EA), the Vario MICRI cube. The morphology of the samples was examined by means of field-emission scanning electron microscopy (FE-SEM, Hitachi, S-4800II, 3 kV). Before the observation, the samples were coated with osmium. The transmission electron microscope (TEM) measurements were made using a Hitachi HF-3300, 300 kV instrument. The powder samples were dispersed in isopropanol and kept in an ultrasonic agitator for 10 min; a drop of the solution was dispersed on a copper grid, dried under a UV lamp, and subjected to TEM measurements. X-ray photoelectron spectroscopy (XPS) measurements were performed using a Thermo-scientific, ESCALAB 250Xi model in an ultrahigh vacuum of 10^{-9} mbar. BET analysis for surface area and pore size distribution was performed using the Micromeritics, ASAP 2020 surface and porosity analyzer.

Electrode Preparation and Electrochemical Measurements. The electrochemical activities (ORR and OER) of the catalysts were evaluated using cyclic voltammetry (CV) and a rotating disc electrode (RDE) in an O_2-saturated 0.1 M KOH electrolyte at a scan rate of 10 mV s^{-1} using a computer-controlled potentiostat (Bio-Logic) with a typical three-electrode system. A 5 mg sample of the catalyst was dispersed in 160 μL of isopropanol and 30 μL of DI water; then, 10 μL of Nafion solution was added, and the contents were dispersed by ultrasonication for approximately 30 min to obtain a homogeneous suspension. The catalyst ink (1.5 μL) was dropped onto the surface of a glassy carbon disk (working electrode, 0.071 cm^2) and dried at room temperature. The working electrode was immersed in a glass cell containing 0.1 M KOH aqueous electrolyte. A platinum coil and saturated calomel electrode (SCE) served as counter and reference electrodes, respectively. All potentials reported in this work were converted from the SCE to the RHE scale using E (RHE) = E (SCE) + 0.998 V in 0.1 M KOH. The ORR activity was measured in an O_2-saturated electrolyte (before using an Ar-saturated electrolyte for background correction under the same conditions) with a potential range from 0.2 to 1.00 V vs RHE at various electrode rotations. For the OER measurement, the potential range was 0.95 to 1.7 V vs RHE with a rotation speed of 1600 rpm. For comparison, the ORR and OER activity was carried out 20 wt % Pt/C (Johnson Matthey), 20% Pt−Ru/C (Johnson Matthey), and IrO_2 (Aldrich) precious metal catalysts. The number of electrons transferred during ORR was calculated using the Koutecky−Levich eq 3.

$$1/J = 1/J_k + 1/(B\omega^2)$$

$$\text{where } B = 0.62nFAv^{-1/6}C_0(D_0)^{2/3} \quad (3)$$

where J is the measured current density, J_k is the kinetic current density, ω is the angular velocity, n is the number of electrons transferred, F is the Faraday constant, A is the electrode area, v

DOI: 10.1021/acscatal.5b00154
ACS Catal. 2015, 5, 3625−3637

is the kinematic viscosity, C_o is the bulk concentration of O_2 (1.2×10^{-6} mol cm^{-3}), and D_o is the diffusion coefficient of O_2 (1.9×10^{-5} cm^2 s^{-1}) in 0.1 M KOH solution.[34,38,39] The ORR and OER Tafel plots were plotted at current I (mA mg^{-1}) versus potential for the CoS_2(400)/N,S-GO, CoS_2 (500)/N,S-GO, and Co_9S_8(600)/N,S-GO; for each plot, the tangent was drawn to find the mass activity (I_o).

■ ASSOCIATED CONTENT

Supporting Information

The Supporting Information is available free of charge on the ACS Publications website at DOI: 10.1021/acscatal.5b00154.

Synthesis of graphene oxide, cobalt thiourea complex, XP spectrum of CoS_2(500)/N,S-GO and comparative oxygen electrode performance of the CoS_2(400)/N,S-GO, CoS_2(400)/Gr, and CoS_2(400) catalysts (PDF)

■ AUTHOR INFORMATION

Corresponding Author

*E-mail: sangarajus@dgist.ac.kr.

Notes

The authors declare no competing financial interest.

■ ACKNOWLEDGMENTS

This work was supported by the DGIST R&D Program of the Ministry of Education, Science and Technology of Korea (15-BD-01).

■ REFERENCES

(1) Cheon, J. Y.; Kim, T.; Choi, Y.; Jeong, H. Y.; Kim, M. G.; Sa, Y. J.; Kim, J.; Lee, Z.; Yang, T.; Kwon, K.; Terasalo, O.; Park, G.; Adzic, R. R.; Joo, S. H. *Sci. Rep.* **2013**, *3*, Article no. 2715.

(2) Zhou, W.; Wu, X. J.; Cao, X.; Huang, X.; Tan, C.; Tian, J.; Liu, H.; Wang, J.; Zhang, H. *Energy Environ. Sci.* **2013**, *6*, 2921−2924.

(3) Suntivich, J.; Gasteiger, H. A.; Yabuuchi, N.; Nakanishi, H.; Goodenough, J. B.; Shao-Horn, Y. *Nat. Chem.* **2011**, *3*, 546−550.

(4) Grimaud, A.; May, K. J.; Carlton, C. E.; Lee, Y. L.; Risch, M.; Hong, W. T.; Zhou, J.; Shao-Horn, Y. *Nat. Commun.* **2013**, *4*, Articleno. 2439.

(5) Laursen, A. B.; Varela, A. S.; Dionigi, F.; Fanchiu, H.; Miller, C.; Trinhammer, O. L.; Rossmeisl, J.; Dahl, S. *J. Chem. Educ.* **2012**, *89*, 1595−1599.

(6) Candelaria, S. L.; Shao, Y.; Zhou, W.; Li, X.; Xiao, J.; Zhang, J. G.; Wang, Y.; Liu, J.; Li, J.; Cao, G. *Nano Energy* **2012**, *1*, 195−220.

(7) Kong, F.; Zhang, S.; Yin, G.; Wang, Z.; Du, C.; Chen, G.; Zhang, N. *Int. J. Hydrogen Energy* **2012**, *37*, 59−67.

(8) Kong, F.; Zhang, S.; Yin, G.; Zhang, N.; Wang, Z.; Du, C. *Electrochem. Commun.* **2012**, *14*, 63−66.

(9) Jung, H. J.; Park, S.; Ganesan, P.; Popov, B. N. *ECS Trans.* **2008**, *16*, 1117−1121.

(10) Guo, K.; Li, Y.; Yang, J.; Zou, Z.; Xue, X.; Li, X.; Yang, H. *J. Mater. Chem. A* **2014**, *2*, 1509−1514.

(11) Narayanamoorthy, B.; Ramanatha Datta, K. K.; Eswaramoorthy, M.; Balaji, S. *ACS Catal.* **2014**, *4*, 3621−3629.

(12) Deng, X.; Tuyuz, H. *ACS Catal.* **2014**, *4*, 3701−3714.

(13) Zhang, G.; Xia, B. Y.; Wang, X.; David Lou, X. W. *Adv. Mater.* **2014**, *26*, 2408−2412.

(14) Suntivich, J.; May, K. J.; Gasteiger, H. A.; Goodenough, J. B.; Shao-Horn, Y. *Science* **2011**, *334*, 1383−1385.

(15) Lin, Z.; Waller, G.; Liu, Y.; Liu, M.; Wong, C. P. *Adv. Energy Mater.* **2012**, *2*, 884−888.

(16) Gullá, A. F.; Gancs, L.; Allen, R. J.; Mukerjee, S. *Appl. Catal., A* **2007**, *326*, 227−235.

(17) Shanmugam, S.; Osaka, T. *Chem. Commun.* **2011**, *47*, 4463−4465.

(18) Lu, Z. J.; Bao, S. J.; Gou, Y. T.; Cai, C. J.; Ji, C. C.; Xu, M. W.; Song, J.; Wang, R. *RSC Adv.* **2013**, *3*, 3990−3995.

(19) Pylypenko, S.; Queen, A.; Olson, T. S.; Dameron, A.; O'Neill, K.; Neyerlin, K. C.; Pivovar, B.; Dinh, H. N.; Ginley, D. S.; Gennett, T.; O'Hayre, R. *J. Phys. Chem. C* **2011**, *115*, 13667−13675.

(20) Peng, H.; Mo, Z.; Liao, S.; Liang, H.; Yang, L.; Luo, F.; Song, H.; Zhong, Y.; Zhang, B. *Sci. Rep.* **2013**, *3*, Article no. 1765.

(21) Hung, T. F.; Tu, M. H.; Tsai, C. W.; Chen, C. J.; Liu, R. S.; Liu, W. R.; Lo, M. Y. *Int. J. Hydrogen Energy* **2013**, *38*, 3956−3962.

(22) Parvez, K.; Yang, S.; Hernandez, Y.; Winter, A.; Turchanin, A.; Feng, X.; Mullen, K. *ACS Nano* **2012**, *6*, 9541−9550.

(23) Su, Q.; Xie, J.; Zhang, J.; Zhong, Y.; Du, G.; Xu, B. *ACS Appl. Mater. Interfaces* **2014**, *6*, 3016−3022.

(24) Zhu, L.; Susac, D.; Teo, M.; Wong, K. *J. Catal.* **2008**, *258*, 235−242.

(25) Sidik, R. A.; Anderson, A. B. *J. Phys. Chem. B* **2006**, *110*, 936−941.

(26) Lyth, S. M.; Nabae, Y.; Moriya, S.; Kuroki, S.; Kakimoto, M.; Ozaki, J.; Miyata, S. *J. Phys. Chem. C* **2009**, *113*, 20148−20151.

(27) Zhao, C.; Li, D.; Feng, Y. *J. Mater. Chem. A* **2013**, *1*, 5741−5756.

(28) Prabu, M.; Ramakrishnan, P.; Shanmugam, S. *Electrochem. Commun.* **2014**, *41*, 59−63.

(29) Wang, H.; Liang, Y.; Li, Y.; Dai, H. *Angew. Chem., Int. Ed.* **2011**, *50*, 10969−10972.

(30) Mahmood, N.; Zhang, C.; Jiang, J.; Liu, F.; Hou, Y. *Chem. - Eur. J.* **2013**, *19*, 5183−5190.

(31) Zhang, L.; Niu, J.; Li, M.; Xia, Z. *J. Phys. Chem. C* **2014**, *118*, 3545−3553.

(32) Liu, Z.; Nie, H.; Yang, Z.; Zhang, J.; Jin, Z.; Lu, Y.; Xiao, Z.; Huang, S. *Nanoscale* **2013**, *5*, 3283−3288.

(33) Kumar, N.; Raman, N.; Sundaresan, A. *Z. Anorg. Allg. Chem.* **2014**, *640*, 1069−1074.

(34) Jo, G.; Shanmugam, S. *Electrochem. Commun.* **2012**, *25*, 101−104.

(35) Roy, R. K.; Shen, S.; Kernion, S. J.; Mchenry, M. E. *Appl. Phys. Lett.* **2011**, *99*, 192506−1−3.

(36) Roy, R. K.; Kernion, S. J.; Shen, S.; McHenry, M. E. *J. Appl. Phys.* **2012**, *111*, 07A301−1−3.

(37) Kim, Y.; Shanmugam, S. *ACS Appl. Mater. Interfaces* **2013**, *5*, 12197−12204.

(38) Liang, Y.; Wang, H.; Zhou, J.; Li, Y.; Wang, J.; Regier, T.; Dai, H. *J. Am. Chem. Soc.* **2012**, *134*, 3517−3523.

(39) Bard, A. J.; Faulkner, L. R.; Swain, E.; Robey, C. *Electrochemical Methods: Fundamentals and Applications*, 2nd ed.; John Wiley & Sons: New York, 2001; pp 1−833.

(40) Chakraborty, I.; Malik, P. K.; Moulik, S. P. *J. Nanopart. Res.* **2006**, *8*, 889−897.

(41) Klaas, J.; Jaeger, N. I. *J. Phys. Chem. B* **1997**, *101*, 1305−1311.

(42) Dang, Y.; Meng, X.; Jiang, K.; Zhong, C.; Chen, X.; Qin, J. *J. Dalton Trans.* **2013**, *42*, 9893−9897.

(43) Yang, Z.; Yao, Z.; Li, G.; Fang, G.; Nie, H.; Liu, Z.; Zhou, X.; Chen, X.; Huang, S. *ACS Nano* **2012**, *6*, 205−211.

(44) Liu, Q.; Jin, J.; Zhang, J. *ACS Appl. Mater. Interfaces* **2013**, *5*, 5002−5008.

(45) Sun, Y.; Liu, C.; Grauer, D. C.; Yano, J.; Long, J. R.; Yang, P.; Chang, C. J. *J. Am. Chem. Soc.* **2013**, *135*, 17699−17702.

(46) Wu, G.; Chung, H. T.; Nelson, M.; Artyushkra, K.; More, K. L.; Johnston, C. M.; Zelenay, P. *ECS Trans.* **2011**, *41*, 1709−1717.

(47) Apostolova, R. D.; Shembel', E. M.; Talyosef, I.; Grinblat, J.; Markovsky, B.; Aurbach, D. *Russ. J. Electrochem.* **2009**, *45*, 311−319.

(48) Lin, V.; Clothup, B. N.; Fateley, G. W.; Grasselli, G. J. *The Handbook of Infrared and Raman Characteristic Frequencies of Organic Molecules*; Elsevier: San Diego, 1991; pp 1−232.

(49) Coates, J. *Interpretation of Infrared Spectra, A Practical Approach*; John Wiley & Sons, Chichester, U.K., 2000; pp 10815−10837.

(50) Gorlin, Y.; Jaramillo, T. F. *J. Am. Chem. Soc.* **2010**, *132*, 13612−13614.

(51) Seo, J.; Cha, D.; Takanabe, K.; Kubotaad, J.; Domen, K. *Phys. Chem. Chem. Phys.* **2014**, *16*, 895.

DOI: 10.1021/acscatal.5b00154
ACS Catal. 2015, 5, 3625−3637

(52) Espejo, A.; Oritix, J.; Rios, Edumundo.; Herrera, F.; Alburquenque, D.; Luis Gautier, J. L. *J. Chil. Chem. Soc.* **2014**, *59*, 2502−2506.
(53) Perez-Alonso, F. J.; McCarthy, D. N.; Nierhoff, A.; Hernandez-Fernandez, P.; Strebel, C.; Stephens, I. E. L.; Nielsen, J. H.; Chorkendorff, I. *Angew. Chem., Int. Ed.* **2012**, *51*, 4641−4643.
(54) Fang, Y. H.; Liu, Z. P. *ACS Catal.* **2014**, *4*, 4364−4376.
(55) Damjanovic, A.; Dey, A.; Bockris, J. O'M. *Electrochim. Acta* **1966**, *11*, 791−874.
(56) Xu, J.; Gaob, P.; Zhao, T. S. *Energy Environ. Sci.* **2012**, *5*, 5333−5339.
(57) M. Hamdani, M.; Singh, R. N.; Chartier, P. *Int. J. Electrochem. Sci.* **2010**, *5*, 556−577.
(58) Chen, Z.; Yu, A.; Ahmed, R.; Wang, H.; Li, H.; Chen, Z. *Electrochim. Acta* **2012**, *69*, 295−300.
(59) Prabu, M.; Ketpang, K.; Shanmugam, S. *Nanoscale* **2014**, *6*, 3173−3181.
(60) Yan, X. H.; Xu, B. Q. *J. Mater. Chem. A* **2014**, *2*, 8617−8622.
(61) Yan, X. Y.; Zhang, G. R.; Xu, B. Q. *Chin. J. of Catal.* **2013**, *34*, 1992−1997.
(62) Rincon, R. A.; Mehrpour, S.; Tietz, F.; Schuhmann, W. *Chem. Commun.* **2014**, *50*, 14760−14762.
(63) Sharma, S.; Pollet, B. G. *J. Power Sources* **2012**, *208*, 96−119.
(64) Cui, Q.; Chao, S.; Wang, P.; Bai, Z.; Yan, H.; Wang, K.; Yang, L. *RSC Adv.* **2014**, *4*, 12168−12174.

DOI: 10.1021/acscatal.5b00154
ACS Catal. 2015, 5, 3625−3637